

# [AstralMikado] Computational simulation of astral cytoskeletal networks reveals optimal architecture for mechanical strength

Brady<sup>a</sup> and Jun<sup>a</sup>

<sup>a</sup>University of California Irvine

## Abstract

A repeated pattern in cytoskeletal architecture is the aster, in which a number of F-actin filaments emerge star-shaped from a central node. Aster-based structures occur in cytoplasmic actin, the early stages of the cytokinetic ring in yeast, and in the context of biomimetic materials engineering. In this work, we use computational simulation to show that there is an optimal number of filaments per aster—what we term the “astral number”—that maximizes rigidity, even at a fixed density of F-actin. This nonlinear dependence holds for both the shear and extensional moduli. Furthermore, we find that increasing astral number leads to dramatic increases in the sample-to-sample variability in network rigidity. We explain both effects using percolation theory, wherein the probability that a given network is productively connected exhibits a sharp dependence on parameters. The dependence of network rigidity on astral number may suggest a mechanism by which cells tune the physical properties of their actin networks and may inform efforts to create adaptive synthetic metamaterials inspired by actin networks.

## Introduction

Make sure to tie in García-Arcos 2024 (Rigidity percolation and active advection synergize in the actomyosin cortex to drive ameboid cell motility)!

### Articulating the gap

- 

### Candidate titles

- (Computational simulation of) the mechanical strength of astral cytoskeletal networks
- Optimal architecture of astral cytoskeletal networks
- Mechanical strength of astral filamentous/fiber/polymer networks
- Computational simulation of the mechanical strength of astral filamentous/fiber/polymer networks

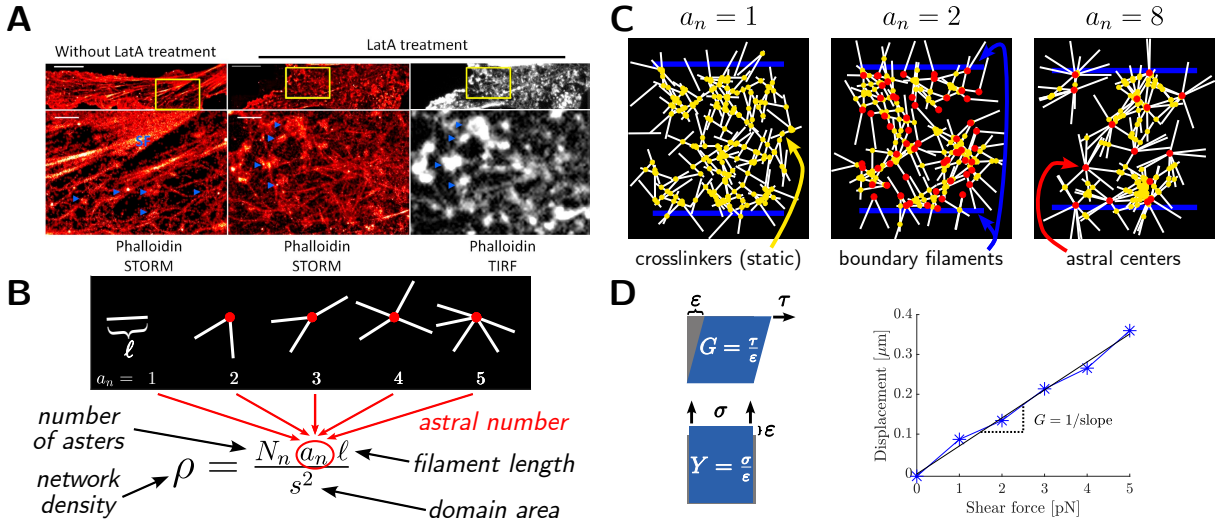


**Figure 1: Framework for studying astral network rigidity.** (a) Images of actin structures before (left) and after (middle, right) treatment with 200 nM of the actin monomer sequestering drug LatA for 20 min in [cell type ambiguous, maybe HeLa JW cells (Paran et al., 2006)?]. Actin structures were visualized via staining with Alexa Fluor 647-phalloidin, which selectively labels F-actin. Stochastic optical reconstruction microscopy (STORM) was used to produce the left and middle images, and the right image represents the same field as the middle panel visualized by total internal reflection fluorescence (TIRF). Blue arrowheads indicate some of the actin nodes. Scale bars: 5 μm (top); 1 μm (bottom). Reproduced with permission from Luo et al. [1]. (b) Schematic of asters and their astral number  $a_n$ , i.e. the number of filaments per central node. Variations in  $a_n$  at a fixed network density  $\rho$  correspond to changes in the microstructural arrangement of a set number of filaments. Astral number 1 is a “degenerate” case, i.e. the unit network element is an individual filament rather than a node associated to multiple filaments. (c) Schematics of filament networks at fixed density  $\rho$  and astral numbers 1 (left), 2 (middle), and 8 (right). Crosslinkers are shown in yellow, boundary filaments are shown in blue, and astral centers are shown in red. (d) Diagram representing the bulk shear modulus  $G$  (left, top) and bulk Young’s modulus  $Y$  (left, bottom). We estimate these elastic moduli via linear regression on a set of (force, displacement) data.

- Optimal architecture of astral filamentous/fiber/polymer networks
- Computational simulation of astral cytoskeletal networks reveals optimal architecture for maximizing mechanical strength and minimizing mechanical failure risk
- Computational simulation of astral cytoskeletal networks reveals optimal architecture for mechanical strength

## Literature

Primarily modeling: Miller et al. [2], Wilhelm and Frey [3]. Some examples of textual citation where we talk about the work of Miller et al. [2], versus parenthetical citation where we mention a fact [2].

## Results

To understand the properties of astral cytoskeletal networks, we extended the model of Wilhelm and Frey [3] to the case of astral network components. Aster are represented in the model as radial assemblies of  $a_n$  filaments per central node (their *astral number*, see Figure 1b), each filament having fixed length  $\ell$ . Every aster in a particular network has the same number of filaments per central node, hence  $a_n$  refers both to the specific microstructure of an aster as well as a class of materials. To form a network,  $N_n$  asters were distributed in a square domain of area  $s^2$  and permanently binding crosslinkers were distributed to crosslink asters to each other and to the boundary at the top and bottom of the domain (Figure 1c). Coordinates of astral centers and the orientation of each filament about its respective center were sampled uniformly at random. We use network density  $\rho$  to refer to the average filament length per unit network area,

$$\rho = \frac{a_n N_n \ell}{s^2}. \quad (1)$$

For the majority of this work we restrict our attention to networks with  $\ell = 1 \mu\text{m}$  and  $s = 10 \mu\text{m}$ ; for a complete list of default parameter values see Table 1.

### Rigidity of astral filamentous networks exhibits a maximum at intermediate astral number, even at fixed density

To study the effect of various astral microstructures on the mechanical properties of disordered filament networks, we simulated networks at fixed density  $\rho$  while varying astral number  $a_n$ . Note this may be viewed as creating a series of networks which contain the same total number of filaments but differ in the smallest allowable network unit (i.e., the number of filaments each aster groups together).

We quantified the rigidity of these astral networks by estimating an elastic modulus from the slope of stress-strain data. To do this, we applied a varying force to each sampled network, computed center-of-mass displacements at steady state, and used linear regression to estimate an elastic modulus (Figure 1d). For a complete description of the mechanical simulation procedure, see Methods. We investigated network behavior under shear and under tension. Representative images of networks experiencing a varying shear force are provided in Figure 2a.

We observed a peak in both the shear and Young's (tensile) moduli at an intermediate astral number (Figure 2b). These peaks in modulus occur at similar astral numbers for both deformation modes. Moreover, the location of such peaks is insensitive to the specific network density tested (Figure S2). The differences in peak height ( $\sim 10 \text{ pN } \mu\text{m}^{-1}$  for shear,  $\sim 100 \text{ pN } \mu\text{m}^{-1}$  for Young's) may indicate that filament bending is less accessible when the networks are under tension.

The sample-to-sample variability in elastic modulus is another prominent feature of Figure 2b. Whereas for non-astral networks ( $a_n = 1$ ) the variance in moduli is low, at moderate astral number the spread of the sampled moduli values appears much larger. This suggests that network rigidity is more sensitive to randomness in the initial configuration of network components when astral number is higher. However, at sufficiently high astral number the mean modulus values fall to near 0. At these astral numbers, filaments are highly concentrated around relatively few nodes, making it extremely unlikely that network components connect into a structure capable of resisting force.

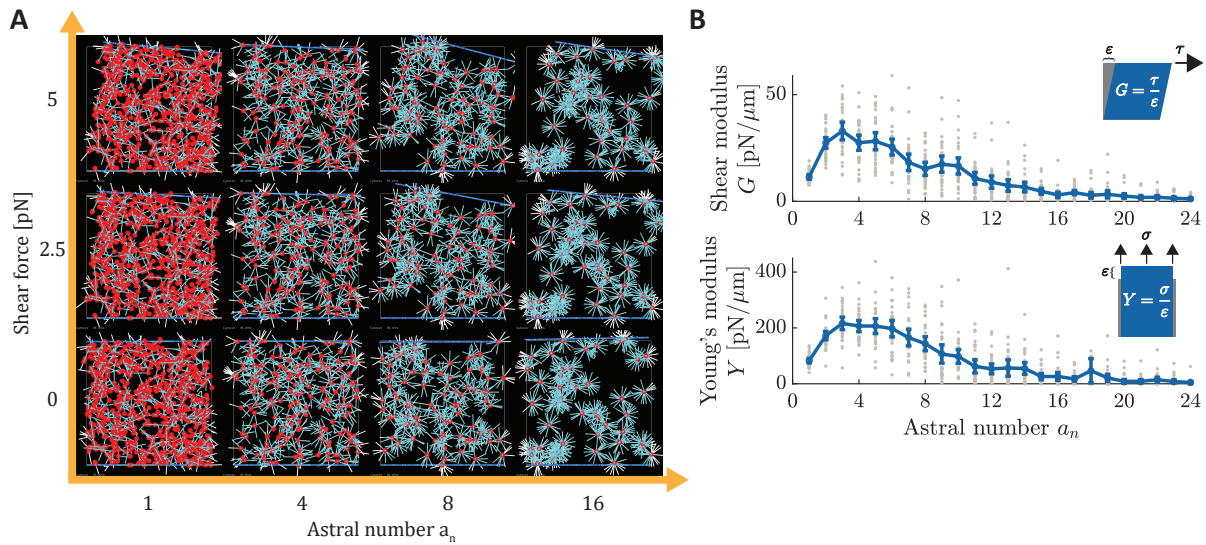


**Figure 2: Rigidity of astral filamentous networks exhibits a maximum at intermediate astral number, even at fixed density.** (a) Steady-state snapshots of astral network deformation in response to applied shear forces. All tiles have equal network density. (b) Elastic moduli of astral networks at density  $\rho = 7.5 \mu\text{m}^{-1}$  as a function of astral number. Upper: shear modulus, lower: Young's (tensile) modulus. Plots show mean and 95% CIs from  $N = 30$  network samples using 6 force values per network (see Methods for details). Individual network moduli are also shown (gray markers). Schematic representations of each modulus are provided for reference.

## Weakening at high astral number is due to increasing probability of network failure

To investigate further the role of geometric variability in determining network rigidity, we sampled a higher number of networks to estimate the distributions of the shear and Young's moduli for various astral numbers (Figure 3a). As in Figure 2b, the data for shear and Young's moduli have very similar shapes, though the values for Young's moduli tend to be an order of magnitude higher than for the shear moduli. For non-astral networks ( $a_n = 1$ ), the distributions of moduli is approximately Gaussian with low variance (purple CDFs and histograms in Figure 3a). For intermediate astral number  $a_n \approx 4$ , the distributions of moduli still have Gaussian character while showing an increase in both the mean and variance of modulus values compared to  $a_n = 1$ . Once astral number increases past this region, the distributions become increasingly skewed towards low modulus values, losing the upward concavity at 0 by  $a_n = 8$  and becoming distinctly exponential by  $a_n = 16$  (yellow-green CDFs and histograms in Figure 3a).

This marked shift from Gaussian to exponential distribution types suggests that increasing  $a_n$  beyond intermediate values results in a bias towards weak and mechanically incompetent networks at these astral numbers. We computed, at each sampled astral number, the proportion of networks which had modulus below half of the respective median modulus value (Figure 3b). For astral numbers below  $\approx 4$ , the proportion of networks which are weak relative to the median is no higher than approximately 5 percent. However, this quantity approaches 30 to 40 percent at high astral numbers, even as the median modulus at high astral numbers itself decreases (intersections with dashed lines in Figure 3a). Thus the weakening at high astral numbers is driven in part by an increase in the likelihood of a network geometry being incapable of withstanding mechanical load (e.g., due to fractures or gaps).

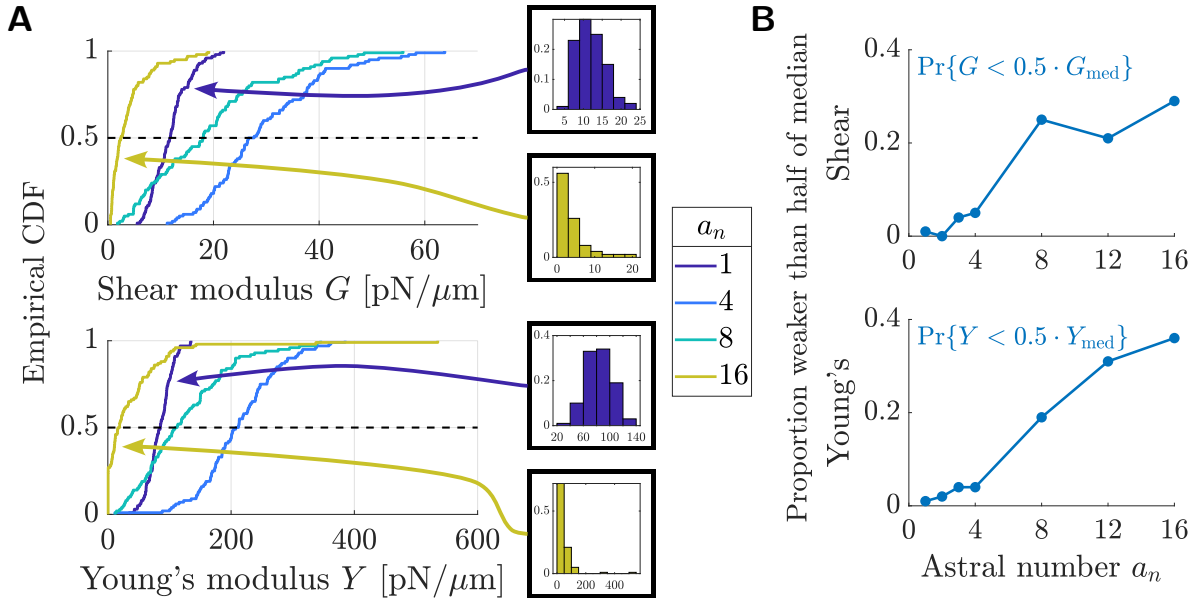


**Figure 3: Weakening at high astral number is due to increasing probability of network failure.** (a) Cumulative distribution functions (CDFs) for the elastic moduli of astral networks at  $\rho = 7.5 \mu\text{m}^{-1}$ . Histograms depict the corresponding probability densities of the indicated distributions. Upper: shear modulus, lower: Young's (tensile) modulus. (b) Probability that an astral network is weak relative to the median network at its astral number. Distributions were estimated from  $N = 100$  network samples using 4 force values per network (see methods for details).

## Strengthening over low astral numbers does not correlate with dangling filament fraction

A possible explanation for why networks with intermediate astral number are more rigid than non-astral networks is that they somehow incorporate more of the available filament length into mechanically productive structures. One way to classify if a filament segment is mechanically productive is to distinguish between filament segments which are bounded on both ends by a crosslink (orange segments in Figure 4a) and those which are not; those in the latter category are known as dangling ends (black segments in Figure 4a). In principle, segments which lie between two crosslinks are capable of transmitting force and storing deformational energy, thus forming the foundation for a mechanically competent network. Dangling ends, however, do not experience any net force when a network is deformed.

To test if changes in dangling end features could explain the initial rigidity increase shown in Figure 2b, we measured the dangling end lengths in networks with different astral numbers (see Methods for details). Distributions of dangling ends have the shape of an exponential distribution with a singular accumulation point corresponding to the maximum dangling end length  $\ell = 1 \mu\text{m}$  (Figure 4b). At sufficiently high astral numbers, this accumulation point gathers enough probability that the distributions appear bimodal. The exponential part of these distributions is in agreement with analytic studies which predict the distribution of dangling ends to be exponential [citation needed].

The mean dangling end length in astral networks increases essentially monotonically with  $a_n$  (Figure 4c). This increase vanishes when inspecting only the dangling ends with lengths strictly below  $\ell$ , showing that the change in mean dangling end length is driven largely by the number of totally isolated filaments. As a complimentary quantification, we computed the length “use fraction” for all sampled networks, defined as 
$$\frac{\text{length not in dangling ends}}{\text{total filament length in network}} = 1 - \frac{\text{total dangling end length}}{\text{total filament length in network}}$$
. While the use fraction increases when  $a_n$  changes from 1 to 2, it decreases consistently for  $a_n \geq 2$ . The initial increase in use fraction is likely because there are fewer total dangling ends in astral networks, since filament ends located at astral centers are considered to be crosslinked to each other precisely at their ends. (In non-astral networks, both ends of a filament generate dangling ends of nonzero length.) Overall, the trends pertaining to dangling ends in astral networks do not correlate well with the modulus trends observed in Figure 2b.

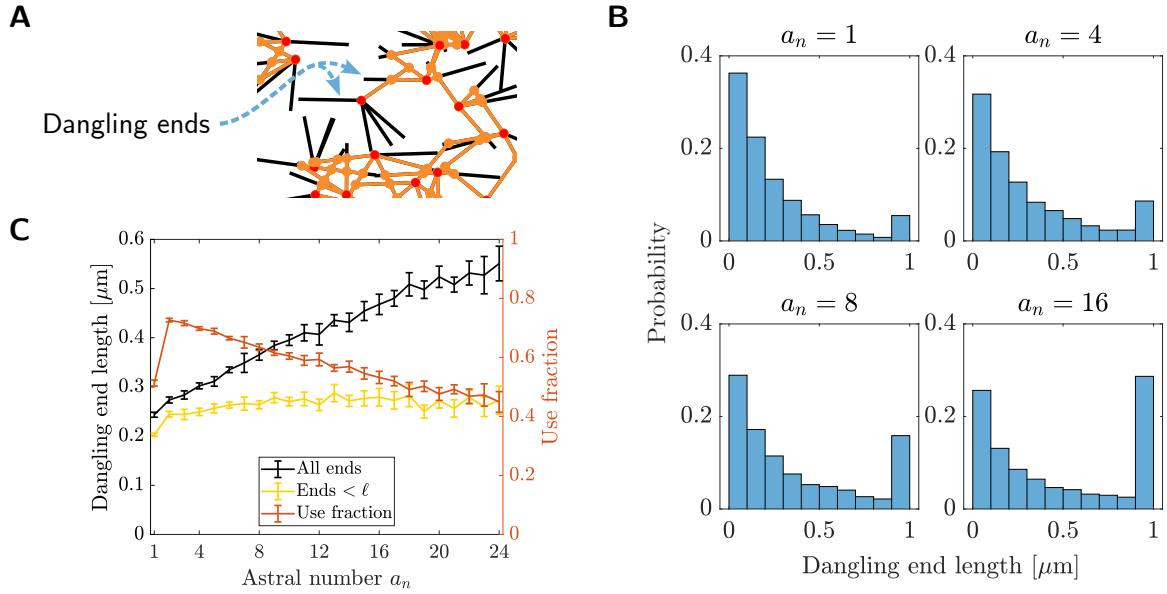
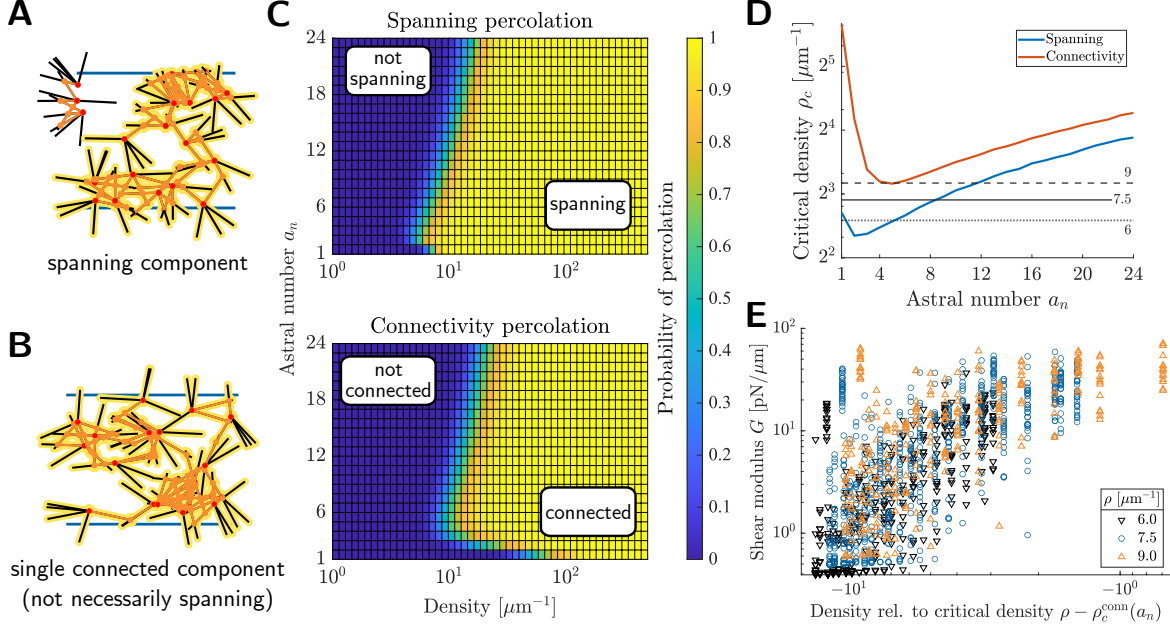


Figure 4: **Strengthening over low astral numbers does not correlate with dangling filament fraction.** (a) Schematic showing dangling ends (black sections of filaments) in astral networks. (b) Histograms of dangling end lengths at various astral numbers. Distributions are aggregated from the dangling ends in 10 networks at each astral number. (c) Mean dangling end length as a function of astral number. Also shown is the length “use fraction”, defined as  $\frac{\text{length not in dangling ends}}{\text{total filament length in network}}$ . Data shown are mean and 95% CIs estimated from 10 networks.

## Mechanical rigidity correlates with network connectedness

While dangling ends do not appear to explain the rigidity properties of astral networks, astral microstructure may modulate network geometry in other ways.



**Figure 5: Mechanical rigidity correlates with network connectedness.** (a) Example of a network with a connected component that spans between the top and bottom edges of the domain. (b) Example of a network where all asters are connected into a single component. (c) Heatmaps showing percolation probabilities for astral networks of size  $s = 10 \mu\text{m}$  with filaments of length  $\ell = 1 \mu\text{m}$ . Probabilities were estimated from  $N = 2000$  networks at each sampled density and astral number. (d) Critical percolation densities estimated from the data in (c) as a function of astral number. The critical percolation density is defined as the network density where the percolation probability reaches 50%. (e) Shear modulus versus  $\Delta\rho = \rho - \rho_c^{\text{conn}}(a_n)$ , the difference between the filament density in the simulated network  $\rho$  and the critical connectivity percolation density  $\rho_c^{\text{conn}}(a_n)$ . Three network densities are shown (see also Figure S2).

## **Discussion**

## Methods

### Mechanical simulations

Mechanical simulations of astral cytoskeletal networks were carried out in Cytosim [4]. Filaments were modeled as inextensible filaments of length  $\ell = 1 \mu\text{m}$  and bending rigidity  $20 \text{ pN } \mu\text{m}^2$ , corresponding to a persistence length of [??]. Filaments were not allowed to grow, shrink, or fracture. Asters group filaments into radial assemblies via the action of two springs at the astral center with stiffnesses  $1000 \text{ pN } \mu\text{m}^{-1}$  and  $500 \text{ pN } \mu\text{m}^{-1}$ . The former pins one end of a filament to the astral center, and the latter resists a filament's rotation about the astral center. Orientations of filaments about each astral center were initialized uniformly at random.

Each astral network consists of a number of asters distributed uniformly at random within a square domain of side length  $s = 10 \mu\text{m}$ . All asters in a particular network have the same number of filaments per central node, and we use the term *astral number* (symbol:  $a_n$ ) to refer to this quantity (see also Figure 1b). In addition to asters, two additional boundary filaments were placed at the top and bottom of the domain. Each boundary filament has length equal to  $s$ , the domain size, and rigidities either  $10^3 \text{ pN } \mu\text{m}^2$  (shear force simulations) or  $10^6 \text{ pN } \mu\text{m}^2$  (tensile force simulations).

Irreversibly binding crosslinkers were distributed randomly over the domain area and have a binding radius of  $0.01 \mu\text{m}$ , diffusivity of  $10 \mu\text{m}^2 \text{ s}^{-1}$ , and (linear) stiffness  $100 \text{ pN } \mu\text{m}^{-1}$ . Crosslinkers do not individually exert torques. Unless otherwise indicated, the number of crosslinkers was specified as  $30 \times$  number of filaments, which at density  $7.5 \mu\text{m}^{-1}$  corresponds to  $225 \text{ particles } \mu\text{m}^{-2}$ . A high density of crosslinkers was selected to encourage binding between filaments before they have time to diffuse away from their initial positions, thus mimicking the simulations of Wilhelm and Frey [3] where crosslinks were placed wherever filaments intersect. Additional crosslinkers were placed near boundary filaments ( $10 \text{ particles } \mu\text{m}^{-1} \cdot s$  at each boundary) to facilitate the connection of the astral network to these boundary filaments. Network components are schematized in Figure 1c. See Table 1 for a summary of the key biophysical parameters used in Cytosim; unless otherwise stated, parameters assume the indicated default value. Parameters related to the numerical scheme are summarized in Table 2.

Each simulation begins by letting network components (asters and crosslinkers) diffuse freely for 5 s, allowing crosslinkers to bind asters together into a particular network geometry. During this time, the top and bottom boundary filaments are held in place. Since crosslinkers diffuse quickly relative to filaments and do not unbind, the network geometry that forms is dictated primarily by the random initialization of aster positions.

To study the response of each network to an applied force, we customized Cytosim to enable the application of force to the ends of particular network fibers. At  $t = 5 \text{ s}$ , the position of each fiber in the network was recorded as the initial state of the network. Simultaneously, the top boundary filament was subjected to a constant applied force and the anchors holding it in place were removed. For shear force simulations, a rightward force was applied to the right-hand end of the top boundary filament. For tensile force simulations, upward forces were applied to each of the left- and right-hand ends of the top boundary filament, each with magnitude half of the reported applied force. While the bottom boundary filament remained pinned, the network was allowed to deform until  $t = 45 \text{ s}$ , by which time most networks achieve steady state (Figure S1a and Figure S1c). At  $t = 45 \text{ s}$ , the position of each fiber in the network was recorded as the final state of the network. Center-of-mass network displacements were computed by averaging the positions of all network fibers at times  $t = 5 \text{ s}$  and  $45 \text{ s}$  and subtracting final position from initial position. Note that

Table 1: **Biophysical parameters**

Parameter (symbol)	Default value	Description
system size ( $s$ )	10 $\mu\text{m}$	side length of square domain
network density ( $\rho$ )	7.5 $\mu\text{m}^{-1}$	average filament length per unit area
filament length ( $\ell$ )	1 $\mu\text{m}$	inextensible; no growth/disassembly/fracture
filament bending rigidity ( $k_{\text{bend}}$ )	20 pN $\mu\text{m}^2$	
astral center stiffness #1	1000 pN $\mu\text{m}^{-1}$	attaches filament ends to center of aster
astral center stiffness #2 ( $k_{\text{rot}}$ )	500 pN $\mu\text{m}^{-1}$	resists filament rotation about center of aster; acts 0.3 $\mu\text{m}$ from center
boundary filament bending rigidity	$1 \times 10^3$ pN $\mu\text{m}^2$ (shear); $1 \times 10^6$ pN $\mu\text{m}^2$ (tensile)	
boundary anchor stiffness	$1 \times 10^3$ pN $\mu\text{m}^{-1}$	fix lower boundary filament in place (and upper boundary during crosslinking phase)
boundary anchor spacing	1 $\mu\text{m}$	anchors placed along lower boundary filament
crosslinker concentration	$\approx 225$ particles $\mu\text{m}^{-2}$	see Methods for details
crosslinker stiffness	100 pN $\mu\text{m}^{-1}$	
crosslinker binding rate	10 $\text{s}^{-1}$	
crosslinker unbinding rate	0	crosslinkers do not unbind
crosslinker diffusivity	$10 \mu\text{m}^2 \text{s}^{-1}$	
crosslinker binding range	0.01 $\mu\text{m}$	
shear force range	0 pN to 5 pN	number of equally spaced force values simulated per network specified in each figure caption
tensile force range	0 pN to 20 pN	number of equally spaced force values simulated per network specified in each figure caption
viscosity	0.01 pN s/ $\mu\text{m}^2$	

Table 2: Cytosim “engine” parameters

Parameter	Default value	Description
time step	0.01 s	
numerical tolerance	0.05	default value, unitless
filament segmentation	0.2 $\mu\text{m}$	length of rigid filament sub-segments
boundary filament segmentation	0.5 $\mu\text{m}$	as above but for boundary filaments
duration of crosslinking phase	5 s	system evolves without any applied force; initial network position recorded at end of this phase
duration of force application phase	40 s	constant applied force; final network position recorded at end of this phase

boundary filaments were excluded from center-of-mass computations. For shear, we used only the horizontal ( $x$ ) component of displacement to estimate an elastic modulus, and in extension we used only the vertical ( $y$ ) component. For representative simulations, see Movie M1, Movie M2, Movie M3, Movie M4 (shear force) and Movie M5, Movie M6, Movie M7, Movie M8 (tensile force). Center-of-mass positions of these networks over time are plotted in Figure S1a and Figure S1c.

### Estimation of elastic moduli

To quantify network rigidity, we subjected each sampled network to a series of applied forces and computed the corresponding center-of-mass displacements. We generated  $N$  (randomly selected) seeds for Cytosim’s random number generator, corresponding to  $N$  unique initial geometries at each astral number. Specification of random seeds in the Cytosim `config.cym` file thus enabled us to apply multiple forces to the same network. For each network, we perform a sweep over  $k$  equally spaced force magnitudes from 0 pN to 5 pN (shear) or 0 pN to 20 pN (tensile). We then construct a force-displacement curve and perform linear regression (with intercept fixed at  $(0, 0)$ ) to estimate an elastic modulus (Figure 1d). We remark that for our system, this fitting method is equivalent to estimating the slope of stress-strain data, since network stress is  $\frac{F_{\text{shear}}}{s}$  (or  $\frac{F_{\text{tens}}}{s}$ ) and strain is  $\frac{\Delta x}{s}$  (resp.  $\frac{\Delta y}{s}$ ). The number of force values used per network is specified in each figure caption.

Note that the regression is performed on all (force, displacement) pairs for each network even when curvature appears in the data samples (see Figure S1b and Figure S1d). Also, though fractured/disconnected networks correspond to a modulus identically equal to 0, we did not attempt to detect if a network was disconnected before assigning a modulus. Instead, as fractured network components that are connected to the top boundary continue moving away from their initial positions at a near-constant speed during the force application phase ( $5 \text{ s} \leq t \leq 45 \text{ s}$ ), fractured networks appear in the data as curves with remarkably high displacements. Thus, performing regression on these points produces a modulus estimate very near zero. In the small number of cases where regression yielded a negative slope (likely due to failure of the network to connect with the top boundary, thus leaving the network subject only to thermal fluctuations), a modulus of 0 was manually assigned.

## Dangling ends measurements and geometric percolation analysis

We used MATLAB [R2024b, ref needed] to study geometric properties of astral networks. We generated astral networks by distributing asters uniformly at random in a square domain and placing crosslinks wherever filaments intersect. All filaments associated to the same aster (i.e., node) were considered to be crosslinked to one another. All measurements of dangling ends were conducted for networks which matched the default networks simulated in Cytosim ( $\rho = 7.5 \mu\text{m}^{-1}$ ,  $\ell = 1 \mu\text{m}$ ,  $s = 10 \mu\text{m}$ ). Network parameters for percolation probability estimates are provided in the relevant figure captions.

All filament segments which were not bounded on both ends by a crosslink were recorded as dangling ends (Figure 4a). Note that for the degenerate case  $a_n = 1$ , each filament may generate up to 2 dangling ends, whereas in properly astral networks  $a_n \geq 2$  only filament segments distal to the astral center generate a dangling end. Other filament segments count towards the reported “use fraction,” the fraction of the total filament length in a network that could potentially store energy from network deformation.

To analyze percolation in astral networks, we used the MATLAB function `conncomp` to identify sets of mutually crosslinked filaments, henceforth referred to as connected components. In the language of graph theory, each network filament is represented by a graph vertex and an edge is drawn between vertices if those filaments were crosslinked together (i.e., if they intersected). A connected component was said to be *spanning* if it contained both a crosslink above and below the network boundaries (see Figure 5a), and an entire network was said to be spanning if it contained at least one spanning component. For *connectivity* percolation, we determined if a network had a unique connected component (see Figure 5b). Note that in this paper, a percolation probability  $p = 1$  indicates that 100% of sampled networks were spanning (or, for connectivity, 100% of sampled networks had a unique connected component).

We define the critical percolation densities  $\rho_c^{\text{span}}(a_n)$  and  $\rho_c^{\text{conn}}(a_n)$  to be the network density at which the percolation probability of networks with astral number  $a_n$  equals 50%. To compute these values, we used the MATLAB function `fit` to compute smoothing spline fits (automatically selected smoothing parameter) to the percolation data. Using these fits, we numerically solved (using MATLAB’s `fsoolve`, default tolerances) for the network density where the percolation probability reaches 50%. Example percolation data and fits are shown in Figure [to be made].

## References

- [1] Weiwei Luo, Cheng-han Yu, Zi Zhao Lieu, Jun Allard, Alex Mogilner, Michael P. Sheetz, and Alexander D. Bershadsky. Analysis of the local organization and dynamics of cellular actin networks. *Journal of Cell Biology*, 202(7):1057–1073, 2013. ISSN 0021-9525. doi: 10.1083/jcb.201210123.
- [2] Callie J. Miller, Demetrios Harris, Robert Weaver, G. Bard Ermentrout, and Lance A. Davidson. Emergent mechanics of actomyosin drive punctuated contractions and shape network morphology in the cell cortex. *PLoS Computational Biology*, 14(9):e1006344, 2018. ISSN 1553-734X. doi: 10.1371/journal.pcbi.1006344.
- [3] Jan Wilhelm and Erwin Frey. Elasticity of Stiff Polymer Networks. *Physical Review Letters*, 91(10):108103, 2003. ISSN 0031-9007. doi: 10.1103/physrevlett.91.108103. URL <https://journals.aps.org/prl/abstract/10.1103/PhysRevLett.91.108103>.
- [4] Francois Nedelec and Dietrich Foethke. Collective Langevin dynamics of flexible cytoskeletal fibers. *New Journal of Physics*, 9(11):427–427, 2007. doi: 10.1088/1367-2630/9/11/427.

# 1 Supplemental material

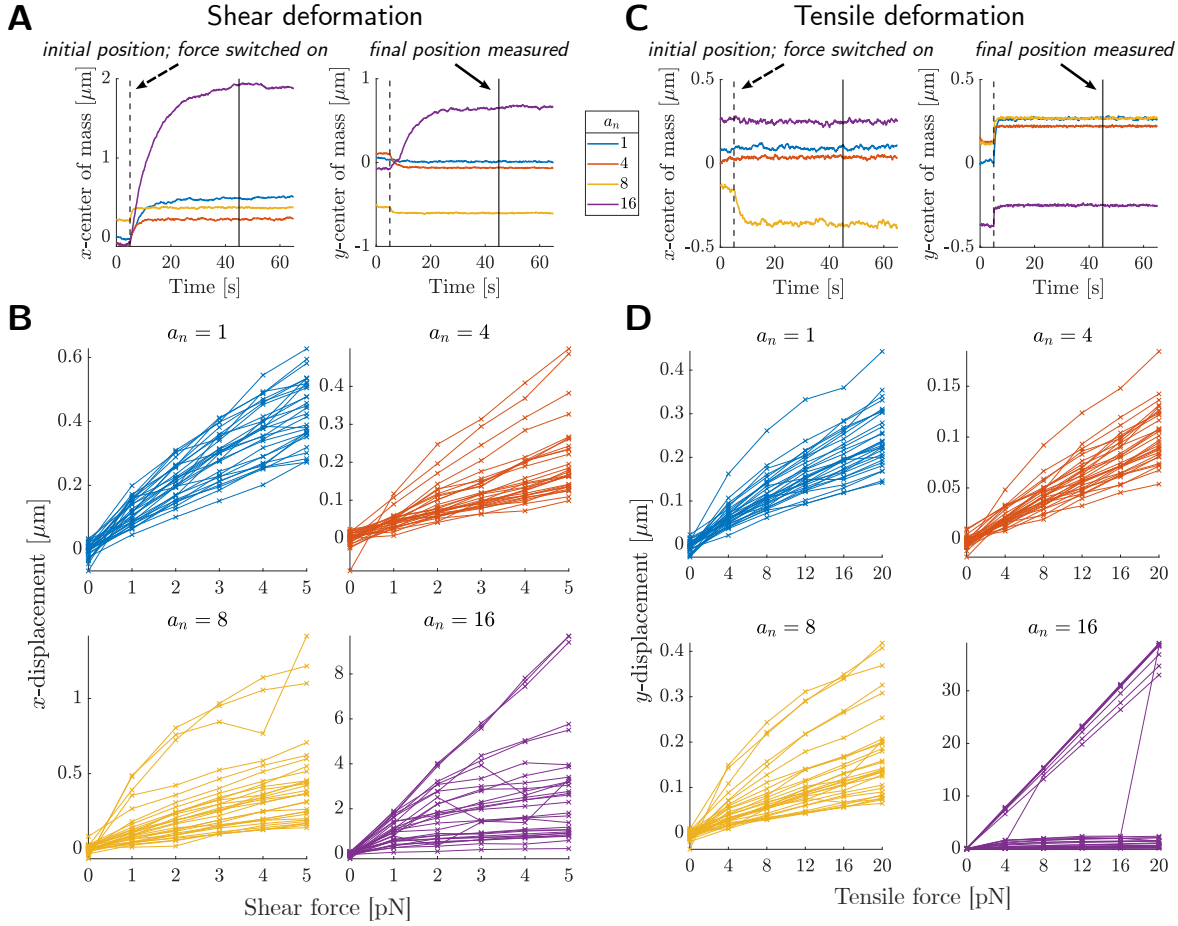


**Figure S1: Force-displacement measurements using Cytosim.** (a) Center of mass coordinates over time for individual networks experiencing a shear force of 5 pN (in the positive  $x$ -direction). Dashed vertical line indicates when the force was switched on, and solid vertical line indicates when final network positions were recorded. Legend is common to (a) and (c). Movies of these networks are provided in M1, M2, M3, and M4. (b) Horizontal displacement data at selected astral numbers (subset of the data used to generate Figure 2b). (c) Center of mass coordinates over time for individual networks experiencing a tensile force of 20 pN (in the positive  $y$ -direction). Dashed vertical line indicates when the force was switched on, and solid vertical line indicates when final network positions were recorded. Movies of these networks are provided in M5, M6, M7, and M8. (d) Vertical displacement data at selected astral numbers (subset of the data used to generate Figure 2b). For (b) and (d),  $N = 30$  networks were simulated per astral number.

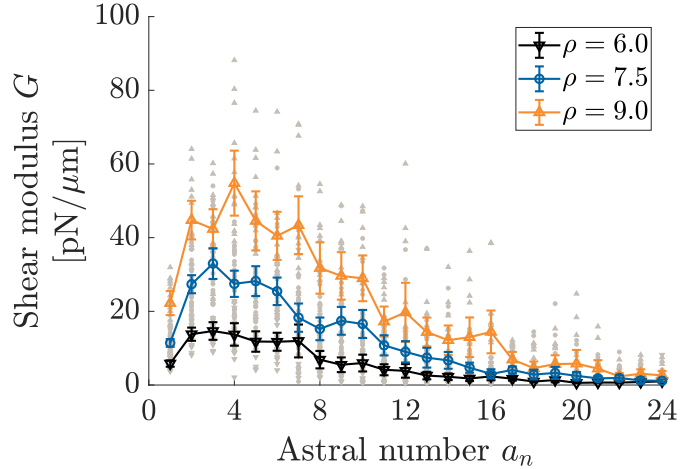


**Figure S2: Location of rigidity peak is insensitive to network density.** Shear modulus as a function of astral number for three filament densities  $\rho$ . Plots show mean and 95% CIs, along with individual network moduli (gray markers). The  $\rho = 7.5 \mu\text{m}^{-1}$  curve is reproduced from Figure 2b, where  $N = 30$  networks were sampled per astral number with 6 force values per network. The curves at  $\rho = 6 \mu\text{m}^{-1}$  and  $\rho = 9 \mu\text{m}^{-1}$  were generated from  $N = 15$  network samples per astral number and 4 force values per network.

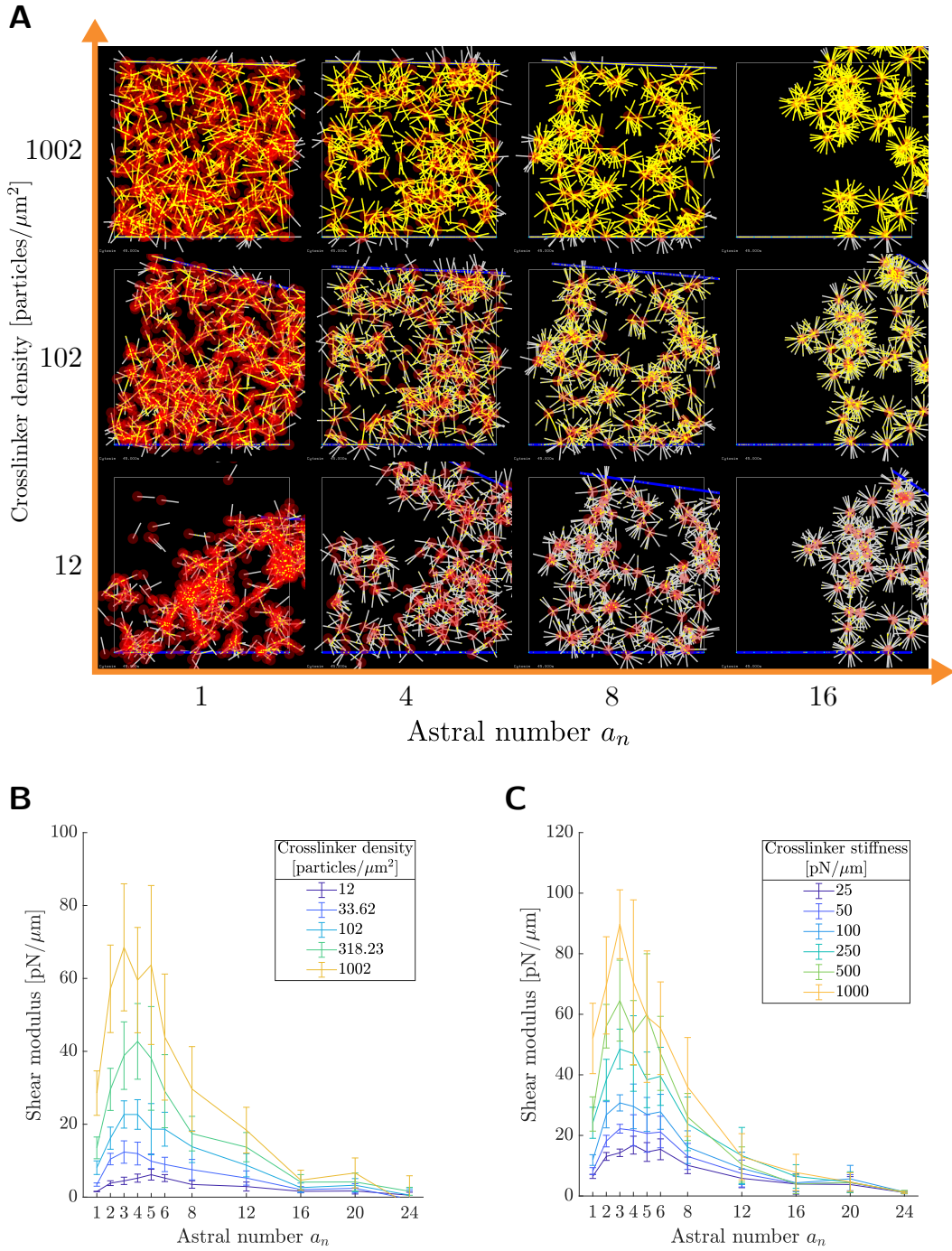


**Figure S3: Rigidity scales similarly with crosslinker density and crosslinker stiffness.** (a) Steady-state snapshots of astral network deformation at various crosslinker densities. Crosslinker particles are shown in yellow, and astral centers are marked in red. All networks have filament density  $\rho = 7.5 \mu\text{m}^{-1}$  and experience a shear force of magnitude 5 pN. (b) Shear modulus as a function of astral number for a series of crosslinker densities. (c) Shear modulus as a function of astral number for a series of crosslinker stiffnesses. Note that “stiffness” refers to the linear stretch resistance of each crosslinker, and crosslinkers do not individually exert torques. Plots show mean and 95% CIs computed from  $N = 10$  networks per astral number and 4 force values per network.

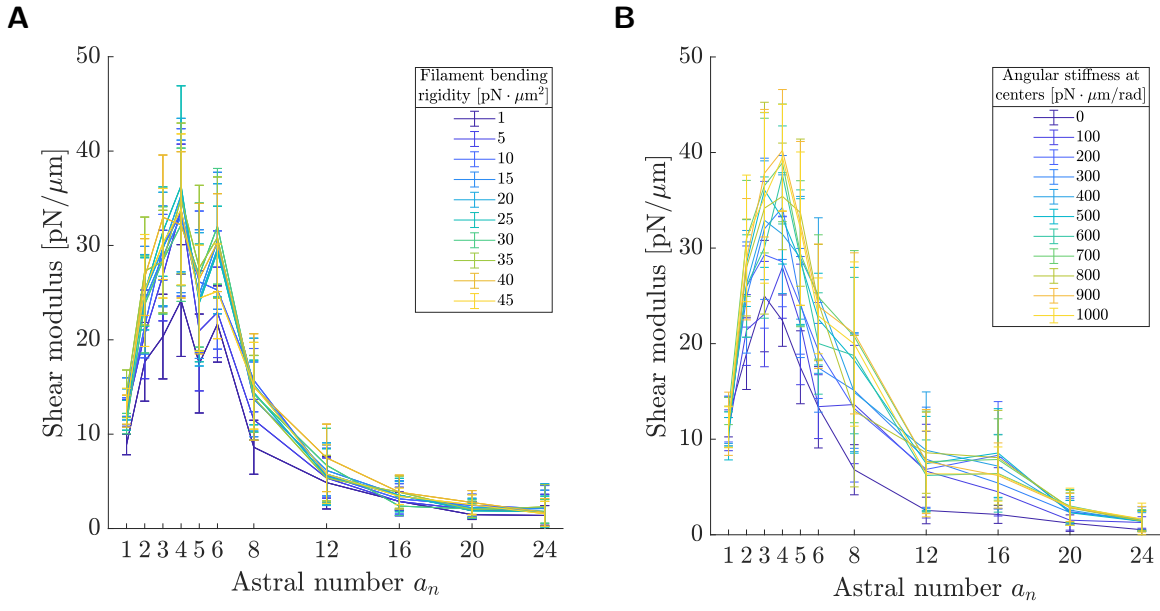


**Figure S4: Peak in stiffness is only weakly sensitive to bending of filaments and angular stiffness at astral centers.** (a) Shear modulus as a function of astral number for a series of filament bending rigidities. A default filament bending rigidity of  $20 \text{ pN} \cdot \mu\text{m}^2$  was used outside of this panel. (b) Shear modulus as a function of astral number for a series of angular stiffnesses at astral centers. A default angular stiffness of  $500 \text{ pN} \cdot \mu\text{m} \cdot \text{rad}^{-1}$  was used outside of this panel. Plots show mean and 95% CIs computed from  $N = 10$  networks per astral number and 4 force values per network.

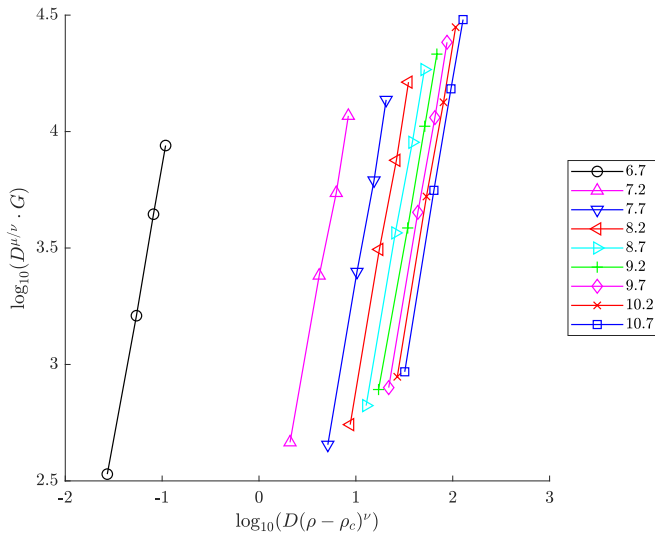


**Figure S5: Domain-size scaling of shear modulus of classical Mikado networks.** Shear moduli of disordered filament networks ( $a_n = 1$ ) for a series of filament densities. Within each curve, domain size  $s$  takes on the values 5  $\mu\text{m}$ , 10  $\mu\text{m}$ , 15  $\mu\text{m}$  and 20  $\mu\text{m}$ . Each plotted point corresponds to a mean modulus estimated from  $N = 15$  networks using 4 force values per network.

## 2 Supplemental Movies

### Shear force

Figure M1: Simulation of a filament network with astral number  $a_n = 1$  (i.e., a classical “Mikado” network) experiencing a shear stress. For times  $0 \leq t < 5$  sec, the network crosslinks into its initial position while no external stress is applied. At time  $t = 5$  sec, a constant shear stress of magnitude  $0.5 \text{ pN } \mu\text{m}^{-1}$  is switched on and maintained for the remainder of the simulation.

Figure M2: Simulation of an astral filament network with astral number  $a_n = 4$  experiencing a shear stress. For times  $0 \leq t < 5$  sec, the network crosslinks into its initial position while no external stress is applied. At time  $t = 5$  sec, a constant shear stress of magnitude  $0.5 \text{ pN } \mu\text{m}^{-1}$  is switched on and maintained for the remainder of the simulation.

Figure M3: Simulation of an astral filament network with astral number  $a_n = 8$  experiencing a shear stress. For times  $0 \leq t < 5$  sec, the network crosslinks into its initial position while no external stress is applied. At time  $t = 5$  sec, a constant shear stress of magnitude  $0.5 \text{ pN } \mu\text{m}^{-1}$  is switched on and maintained for the remainder of the simulation.

Figure M4: Simulation of an astral filament network with astral number  $a_n = 16$  experiencing a shear stress. For times  $0 \leq t < 5$  sec, the network crosslinks into its initial position while no external stress is applied. At time  $t = 5$  sec, a constant shear stress of magnitude  $0.5 \text{ pN } \mu\text{m}^{-1}$  is switched on and maintained for the remainder of the simulation.

### Extensional force

Figure M5: Simulation of a filament network with astral number  $a_n = 1$  (i.e., a classical “Mikado” network) experiencing a tensile stress. For times  $0 \leq t < 5$  sec, the network crosslinks into its initial position while no external stress is applied. At time  $t = 5$  sec, a constant tensile stress of magnitude  $2 \text{ pN } \mu\text{m}^{-1}$  is switched on and maintained for the remainder of the simulation.

Figure M6: Simulation of an astral filament network with astral number  $a_n = 4$  experiencing a tensile stress. For times  $0 \leq t < 5$  sec, the network crosslinks into its initial position while no external stress is applied. At time  $t = 5$  sec, a constant tensile stress of magnitude  $2 \text{ pN } \mu\text{m}^{-1}$  is switched on and maintained for the remainder of the simulation.

Figure M7: Simulation of an astral filament network with astral number  $a_n = 8$  experiencing a tensile stress. For times  $0 \leq t < 5$  sec, the network crosslinks into its initial position while no external stress is applied. At time  $t = 5$  sec, a constant tensile stress of magnitude  $2 \text{ pN } \mu\text{m}^{-1}$  is switched on and maintained for the remainder of the simulation.

Figure M8: Simulation of an astral filament network with astral number  $a_n = 16$  experiencing a tensile stress. For times  $0 \leq t < 5$  sec, the network crosslinks into its initial position while no external stress is applied. At time  $t = 5$  sec, a constant tensile stress of magnitude  $2 \text{ pN } \mu\text{m}^{-1}$  is switched on and maintained for the remainder of the simulation.